Talanta xxx (xxxx) xxx

Contents lists available at ScienceDirect

Talanta

journal homepage: www.elsevier.com/locate/talanta

Diagnostics of SARS-CoV-2 infection using electrical impedance spectroscopy with an immunosensor to detect the spike protein

Juliana C. Soares [a,1], Andrey C. Soares [b,1], Monara Kaelle S.C. Angelim [c], Jose Luiz Proença-Modena [c,d], Pedro M. Moraes-Vieira [c,d,e,2], Luiz H.C. Mattoso [b], Osvaldo N. Oliveira Jr [a,*]

[a] São Carlos Institute of Physics (IFSC), University of São Paulo (USP), 13566-590, São Carlos, Brazil
[b] Nanotechnology National Laboratory for Agriculture (LNNA), Embrapa Instrumentação, 13560-970, São Carlos, SP, Brazil
[c] Department of Genetics, Evolution, Microbiology and Immunology, Institute of Biology, University of Campinas, 13083-862, Campinas, SP, Brazil
[d] Experimental Medicine Research Cluster (EMRC), University of Campinas, 13083-862, Campinas, SP, Brazil
[e] Obesity and Comorbilities Research Center (OCRC), University of Campinas, 13083-862, Campinas, SP, Brazil

ARTICLE INFO

Keywords:
SARS-CoV-2
Immunosensors
Spike protein
Impedance spectroscopy
Information visualization

ABSTRACT

Mass testing for the diagnostics of COVID-19 has been hampered in many countries owing to the high cost of the methodologies to detect genetic material of SARS-CoV-2. In this paper, we report on a low-cost immunosensor capable of detecting the spike protein of SARS-CoV-2, including in samples of inactivated virus. Detection is performed with electrical impedance spectroscopy using an immunosensor that contains a monolayer film of carboxymethyl chitosan as matrix, coated with an active layer of antibodies specific to the spike protein. In addition to a low limit of detection of 0.179 fg/mL within an almost linear behavior from 10^{-20} g/mL to 10^{-14} g/mL, the immunosensor was highly selective. For the samples with the spike protein could be distinguished in multidimensional projection plots from samples with other biomarkers and analytes that could be interfering species for healthy and infected patients. The excellent analytical performance of the immunosensors was validated with the distinction between control samples and those containing inactivated SARS-CoV-2 at different concentrations. The mechanism behind the immunosensor performance is the specific antibody-protein interaction, as confirmed with the changes induced in C–H stretching and protein bands in polarization-modulated infrared reflection absorption spectra (PM-IRRAS). Because impedance spectroscopy measurements can be made with low-cost portable instruments, the immunosensor proposed here can be applied in point-of-care diagnostics for mass testing even in places with limited resources.

1. Introduction

The coronavirus pandemic (COVID-19) caused by SARS-CoV-2 [1–3] has been difficult to manage in countries where mass testing was not made possible due to restrictions related to cost and/or availability of diagnostic tests. Owing to the infection characteristics, distinct tests need to be performed for diagnostics and for monitoring infected people in epidemiological studies [4]. For diagnostics the prevailing tests include detection of genetic material as SARS-CoV-2 is a single-stranded RNA envelope virus [5], for which the most well-established method is real time polymerase chain reaction (RT-PCR) [6,7]. Diagnosis of SARS-CoV-2 infection is then performed with samples of saliva or nasopharyngeal swabs. Clustered regularly interspaced short palindromic repeats (CRISPR) and loop-mediated isothermal amplification (LAMP) are other methods suitable for this type of detection, though less popular. With regard to the identification of an immune response and in epidemiological studies to verify the coverage of immunization, immunoenzymatic assays or agglutination tests have been used [7,8]. For diagnostics at early stages – even before symptoms appear – an alternative to RT-PCR or RT-LAMP is to employ genosensors that may detect genetic material in a faster manner, especially because amplification steps are not required [9]. Unfortunately, genosensors are not

* Corresponding author.
E-mail address: chu@ifsc.usp.br (O.N. Oliveira Jr).
[1] J.C.S. and A.C.S. contributed equally to this work.
[2] Covid-19 International Research Team (COV-IRT)

https://doi.org/10.1016/j.talanta.2021.123076
Received 25 August 2021; Received in revised form 9 November 2021; Accepted 16 November 2021
Available online 22 November 2021

available commercially for SARS-CoV-2 as yet, probably because this type of biosensor has not been exploited with mass production even for other diseases.

Diagnostics of SARS-CoV-2 infection at early stages can also be made with immunosensors since the virus surface is covered by glycosylated spike proteins that bind to cell receptors such as human angiotensin-converting enzyme 2 (hACE2) [10,11]. The latter receptor is expressed in lung cells, alveolar cells, endothelial cells, blood vessels, gastrointestinal and liver cells [3]. Unlike the case of immunosensors to detect antibodies generated in infected patients, which are only effective during some time periods and after several days of the infection as the disease evolves [4], detection of spike proteins can be suitable for diagnostics. For the presence of the spike proteins is a clear indicator of infection as is the case of the genetic material detected by genosensors or with RT-PCR. This has actually been exploited for SARS-CoV-2 [12–18].

In this paper, we report on a simple, low-cost method to detect the spike protein, which is based on impedance spectroscopy applied to an immunosensor. The latter was fabricated on interdigitated gold electrodes coated with a monolayer film of carboxymethyl chitosan onto which an active layer of antibodies was adsorbed. Detection was possible in commercial samples of the spike protein and in real samples of inactivated SARS-CoV-2. The selectivity of the sensor was evaluated using information visualization techniques, including the multidimensional projection interactive document mapping (IDMAP) [19].

2. Experimental section

2.1. Materials

Potassium chloride (KCl), sodium chloride (NaCl), magnesium chloride ($MgCl_2$), anhydrous sodium phosphate dibasic (Na_2HPO_4), anhydrous potassium phosphate monobasic (KH_2PO_4) were obtained from Synth (Brazil). The reagents were of analytical grade and used without further purification. Phosphate buffered saline (PBS) solutions were prepared with 137×10^{-3} mol L^{-1} NaCl, 10^{-3} mol L^{-1} $Na_2{\cdot}HPO_4$, 1.7×10^{-3} mol L^{-1} KH_2PO_4, 2.7×10^{-3} mol L^{-1} KCl (pH 7.4) with addition of 10^{-3} mol L^{-1} $MgCl_2$ (PBS/$MgCl_2$ solution). *N*-(3-dimethylaminopropyl)-*N*′-ethylcarbodiimide hydrochloride (EDC) and *N*-hydroxysuccinimide (NHS) were purchased from Sigma Aldrich. High-purity deionized water (resistivity of 18.2 MΩcm) was obtained from a Milli-Q system (Millipore, USA). Experiments were performed at room temperature (~25 °C). For molecular architecture fabrication, carboxymethylchitosan (CMCt) was purchased from Dayang Chemicals (China). The spike protein and its corresponding antibody were acquired from ABCAM, USA. The real samples of inactivated virus were obtained as follows. HIAE-02 SARS-CoV-2/SP02/human/2020/BRA (GenBank: 616 MT126808.1) virus was isolated from the second confirmed case in Brazil. The stocks of SARS-CoV-2 virus were propagated in Vero cell lines and the supernatant was harvested at 2–3 days post-infection. The viral titers were determined by plaque assays on Vero cells, in which the number of plaque-forming units (PFU) represents the viral quantity. Vero CCL-81 cells were cultivated in MEM supplemented with 10% heat inactivated fetal bovine serum (FBS) and 1% Penicillin-Streptomycin, and incubated at 37 °C with 5% CO_2 atmosphere. As control, we used the conditioned medium of Vero cells which were treated the same way but without the virus. Inactivation of the virus was performed by ultraviolet irradiation in a safety cabinet, following the procedures of Patterson et al. [20].

2.2. Preparation of biosensors

Interdigitated Au electrodes were produced at the National Nanotechnology Laboratory (LNNano/CNPEM) using conventional photolithography. They had 50 pairs of interdigits 10 μm wide, 10 μm apart from each other, so that a capacitive profile was obtained [21,22,23]. Prior to the deposition of the 150 nm Au layer, the glass slides were pre-coated with a 20 nm chromium adhesive layer, following the procedures of Soares et al. [24]. The interdigitated electrodes were coated with a monolayer film of CMCt, formed by immersing the electrodes during 10 min in a CMCt solution (1 mg/mL) at room temperature. They were then immersed in an aqueous solution with 100×10^{-3} mol L^{-1} EDC and 100×10^{-3} mol L^{-1} NHS for 30 min at room temperature to increase the antibody attachment on the carboxylic groups of chitosan sites. To complete the biosensor fabrication, the devices were immersed in a solution with antibodies (ABCAM, USA) (1 ng/mL) in PBS buffer for 30 min at room temperature. Fig. 1 illustrates the functionalization of a modified interdigitated electrode with a CMCt monolayer and the active layer of antibodies for detection of the spike protein.

2.3. Detection

The experiments with commercial samples of the spike protein were conducted by immersing the biosensors for 10 min into 250 μL of various concentrations, viz. 10^{-20} mol L^{-1}, 10^{-18}, 10^{-16}, 10^{-14}, 10^{-12}, 10^{-10}, and 10^{-8} mol L^{-1}. They were then washed with PBS. Control experiments were performed with possible interferents. We have chosen the widely-used drugs fluoxetine (20 mg) (Teuto, Brazil), paracetamol (200 g/mL) (Johnson & Johnson from Brazil, Brazil), nitazoxanide (500 mg) (Mantecorp Farmasa, Brazil) and antigens related to different types of cancer, including carbohydrate antigen 19–9 (CA19-9) (Aviva System Biology, USA), the tumor protein 53 (p53) (Dako, USA), and the human epidermal growth factor receptor 2 (HER2) (Thermo Fischer Scientific, USA). In the experiments with inactivated SARS-CoV-2, the biosensors were immersed for 10 min into solutions containing different concentrations: 7.0×10^{-3}, 7.0×10^{-2}, 7.0×10^{-1}, 7.0×10^{1}, 7.0×10^{2}, 7.0×10^{3}, 7.0×10^{4} and 7.0×10^{5} PFU/mL (PFU = plaque-forming unit per milliliter). The electrical impedance measurements were carried out with an impedance analyzer 1260A (Solartron Analytical) in the frequency range from 1 Hz to 1 MHz with DC 0 mV potential and AC 50 mV potential.

The mechanism responsible for detecting the spike protein was elucidated with polarized-modulated infrared reflection absorption spectroscopy (PM-IRRAS) [25,26], using a PMI 550 spectrophotometer (KSV Instruments) [27]. The measurements were performed with angle of incidence 81° and the spectral resolution 8 cm^{-1}. The CMCt spectrum was used as a reference and the signal was obtained from Eq. (1), where Rp and Rs are the components parallel and perpendicular to the plane of incidence of IR light, respectively [28,29].

$$\frac{\Delta R}{R} = \frac{R_p - R_s}{R_p + R_s} \tag{1}$$

The impedance data were analyzed with the multidimensional projection technique referred to as Interactive Document Mapping (IDMAP) [19], which is useful to evaluate selectivity and false positives. IDMAP projects the capacitance spectra $\mathbf{x_i} = (x_{i1}, x_{i2}, \ldots, x_{in})$ onto a 2D map using the Euclidean distances between data instances in the original space $\delta(x_i, x_j)$. The instances of the projected data $\mathbf{y_i} = (y_{i1}, y_{i2}, \ldots, y_{in})$ are separated from each other by the Euclidean distance $d(yi, yj)$[30]. These projections follow an injective function f: X → Y, which given by Eq (2), where δ_{max} and δ_{min} denote the maximum and minimum distance values between the data instances in the original representation space [30].

$$Error_{IDMAP} = \frac{\delta(x_i, x_j) - \delta_{min}}{\delta_{max} - \delta_{min}} - d(y_i, y_j) \tag{2}$$

3. Results and discussion

Detection of SARS-CoV-2 spike protein could be made by analyzing the capacitance spectra in Fig. 2 where the capacitance was calculated from the measured impedance. The most significant changes in capacitance as the concentration of the spike protein was altered occurred at

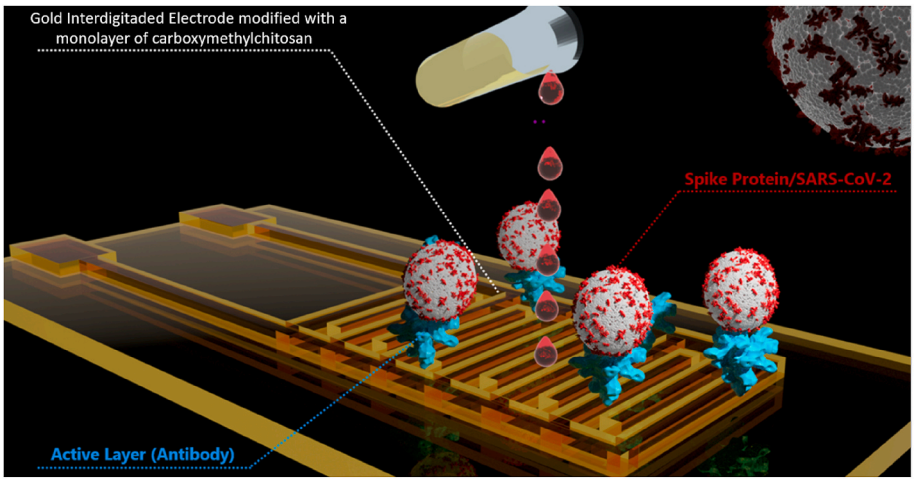

Fig. 1. Gold interdigitated electrode (IDE) modified with a CMCt monolayer and the active layer of antibodies for detecting the spike protein. (For interpretation of the references to color in this figure legend, the reader is referred to the Web version of this article.)

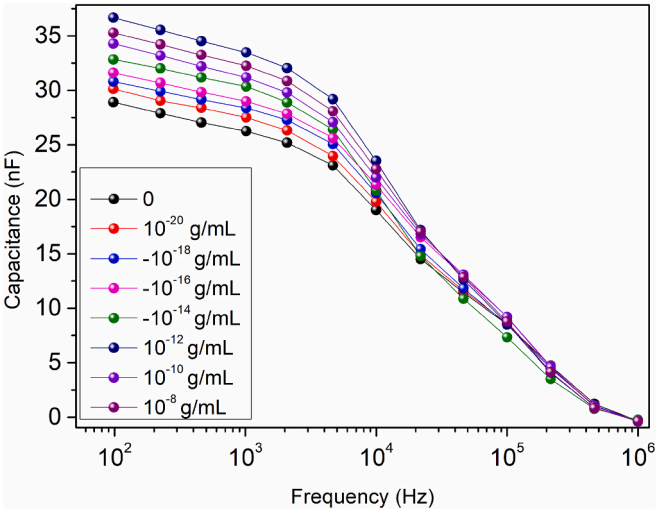

Fig. 2. Capacitance spectra measured with the biosensor immersed in PBS solutions with various spike protein concentrations.

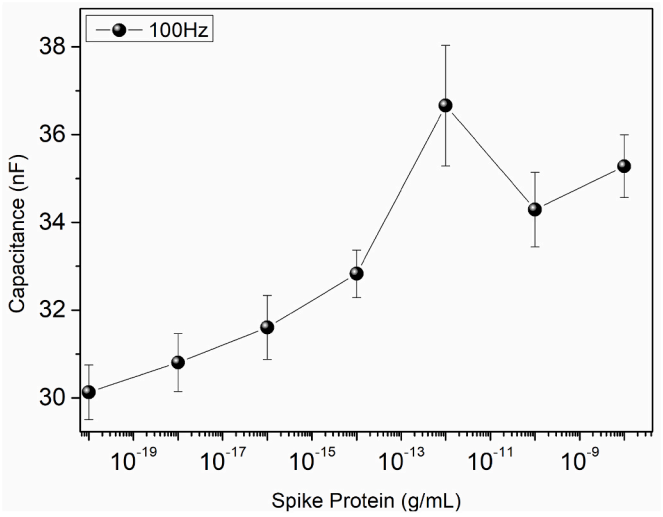

Fig. 3. Calibration curve taken from the data in Fig. 1 at 100 Hz. The immunosensor was immersed in PBS solutions with different concentrations of the spike protein.

low frequencies, as is typical for impedance-based sensors since the electrical response is governed by double-layer effects at such frequencies [31,32,33]. The calibration curve from the capacitance at 100 Hz in Fig. 3 indicates an almost linear increase with the logarithm of the spike protein concentration from 10^{-20} g/mL to 10^{-8} g/mL, with an outlier for the 10^{-12} g/mL samples. The logarithmic dependence is typical of biosensors since the number of available sites for spike protein adsorption tends to zero as the concentration increases [27]. The limit of detection (LOD) is 0.179 fg/mL calculated using the IUPAC method defined in Eq. (3). This value is lower than for the biosensors in the literature [12-17] and competitive with the device developed by Rahmadi et al. [18], being also sufficient to detect SARS-CoV-2 virus in real samples, as demonstrated later on.

$$\mathrm{LoD} = S_{\mathrm{blank}} + (3 \times \mathrm{SD}) \tag{3}$$

where S_{blank} is the signal of a control sample, and SD is the standard deviation.

The frequency 100 Hz was selected for the calibration curve based on an analysis of the distinguishing ability of the biosensor at different frequencies, using the parallel coordinates technique [34]. In this technique, the data from the capacitance spectra are plotted with the normalized capacitance in the ordinate, as in Fig. 4 with different colors to represent the distinct protein concentrations. The distinction ability is quantified through the silhouette coefficient (S) defined in Eq. (4)

$$S = \frac{1}{n}\sum_{i=1}^{n}\frac{(b_i - a_i)}{\max(b_i, a_i)} \tag{4}$$

where **n** is the number of samples, $\mathbf{a_i}$ is the average Euclidean distance calculated between the ith projection and the remaining projections for the capacitance spectra, and $\mathbf{b_i}$ is the minimum distance of the ith projection and other projections with different concentrations [24]. S varies from −1 to 1, where S~1 means full sample differentiation for each frequency (blue boxes), S ~ -1 indicates that the capacitance data are deleterious for distinction (red boxes) and S ~ 0 (white boxes) for data which are indifferent for distinction [35]. The large number of blue boxes indicates that the biosensor with a CMCt matrix has a high distinguishing ability in the spectra region related to the electrical double layer, generated by biorecognition. The average silhouette coefficient calculated with the entire frequency range for this biosensor was 0.757, confirming the ability to detect the spike protein.

The excellent analytical performance of the immunosensor was

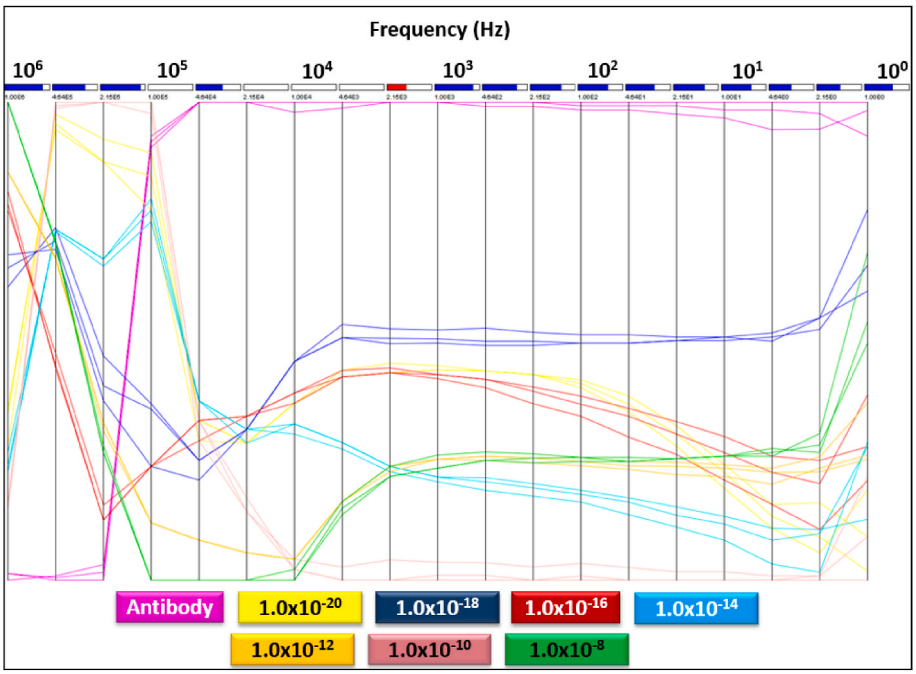

Fig. 4. Parallel Coordinates plot for the data obtained with the biosensor for different concentrations of the spike protein. The x-axis corresponds to the angular frequency while the y-axis corresponds to normalized capacitance values.

confirmed by plotting the capacitance data using the IDMAP technique [19], where each spectrum is represented by a marker on a 2D map. Of particular relevance is the robustness of the biosensor detection against interferents, whose data are also plotted. Fig. 5 shows that the samples with the various concentrations of the spike protein are easily distinguishable from each other and from the data of the molecules used in control experiments, namely CA19-9 protein, p53 protein, HER2 protein, fluoxetin, nitazoxanide, and paracetamol. The data points related to these latter molecules are located at the left part of the map, while the points from the spike protein samples were positioned toward the right with increasing concentrations. In a further test of possible effects from interferents we measured the spectra of solutions containing spike protein and the various interferents. The IDMAP plot in Fig. S1 in the Supporting Information shows that the samples with mixed components (spike protein + interferent) could be easily distinguished from those of the interferents alone, and were located in the same region of the samples containing only the spike protein.

3.1. *Validation of spike protein detection in inactivated SARS-CoV-2 virus*

The analytical performance of the biosensor optimized with detection of spike protein commercial samples was validated in real samples of inactivated SARS-CoV-2 virus. Capacitance spectra were obtained with the biosensor for concentrations of SARS-CoV-2 from 7.0×10^{-3} up to 7.0×10^{5} PFU/mL, which are shown in Fig. S2 in the Supporting Information. As one could have expected from the complexity and variability of the virus samples, it was not possible to determine the limit of detection with an analytical curve. Hence, computational methods

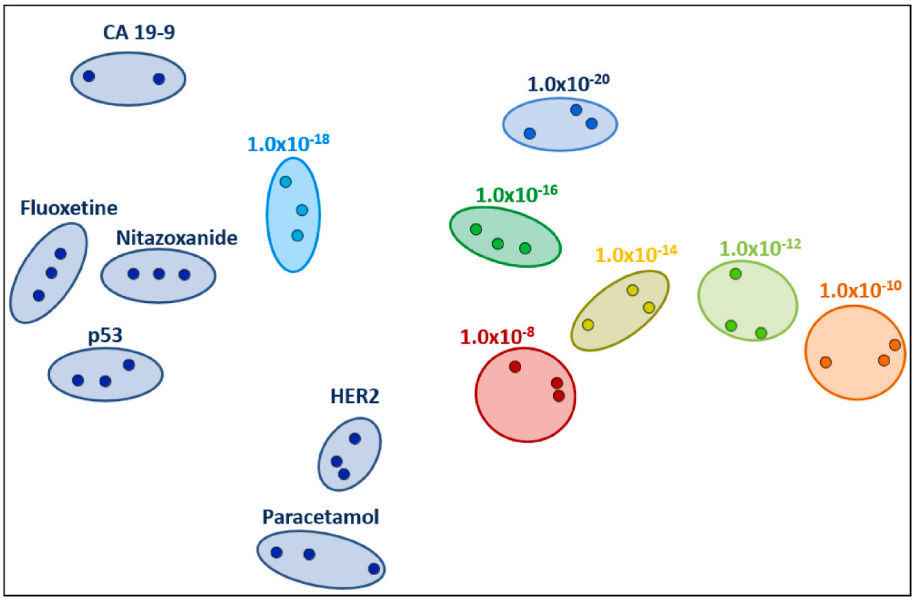

Fig. 5. IDMAP projection of the capacitance spectra obtained for different spike protein concentrations, using biosensors constructed with CMCt monolayer. Also shown are the data points for the possible interferents and other protein molecules. The clusters assigned to the spike protein are separated from the control samples, with the exception of the 10^{-18} g/mL as this is close to the limit of detection. In the IDMAP projection, no labels are assigned to the axes because the useful information is the relative distance between data instances.

were required to analyze the spectra, which we have done using IDMAP in Fig. 6. The distinction ability of the immunosensor is inferred from the IDMAP plot where samples with increasing concentrations are positioned further away from the control sample (without the virus). The overall distinction ability led to a silhouette coefficient (S) 0.581 and various frequencies were adequate for detection, as indicated in the parallel coordinate plot in Fig. S3 in the Supporting Information.

3.2. Mechanism behind spike protein detection

The results in the last subsections confirmed that biosensors constructed with a CMCt matrix and containing an active layer of antibodies are efficient to detect the spike protein, with high sensitivity, selectivity and without false positives. This selectivity is believed to occur due to biorecognition between the active layer and the spike protein, and this was confirmed with the PM-IRRAS spectra in Fig. 7. The PM-IRRAS measurements were performed on gold substrates coated with a CMCt monolayer, whose spectrum was taken as a reference. Following the literature [36–39], we may assign the characteristic bands of proteins, present in the active layer (antibodies) and spike protein, to δ CH_3 at 1382 cm^{-1}, δ C–H from CH_2 at 1478 cm^{-1}, amide II (60% N–H bonds and 40% C–N bonds) at 1570 cm^{-1} and amide I (80% carbonyl stretch (C═O), 10% C–N stretch and 10% N–H bond vibration) [35,37,38,40] at 1647 cm^{-1} (Fig. 6a). The bands assigned to the methylene chains, i.e. δ C–H dipoles from CH_3 and CH_2 groups are seen at 2835 cm^{-1} and 2907 cm^{-1} [39,40]. The antibody-spike protein interaction affects especially the C–H stretching bonds, in addition to some changes in intensity of the protein bands. The changes are not monotonic with the spike protein concentration, which means that molecular reorientation occurs during the interaction. This explanation is based on the fact that the intensity of PM-IRRAS bands depends not only on the presence of the corresponding groups but also on their orientation [41].

4. Conclusions

In this paper we demonstrated that immunosensors can be used in the diagnostics of SARS-CoV-2 infection using electrical impedance spectroscopy, with low-cost methodologies. The high sensitivity achieved with the immunosensor made with a matrix of carboxymethyl chitosan monolayer film, and then coated with an active layer of antibodies, was sufficient to detect the spike protein in inactivated SARS-CoV-2. Using IDMAP to analyze the impedance data, we also confirmed that the immunosensors are selective for the spike protein, which could be distinguished from other proteins and analytes (e.g. pharmaceutical drugs) that could be interfering species as they may be present in samples of healthy or infected patients. The sensitivity and selectivity of the immunosensor can be attributed to the strong antibody-protein specific interaction investigated with PM-IRRAS. With the latter vibration spectroscopy method, it was possible to identify the main bands of spike protein, and infer how the adsorption of said protein affected the bands assigned to the antibodies in the active layer of the immunosensor.

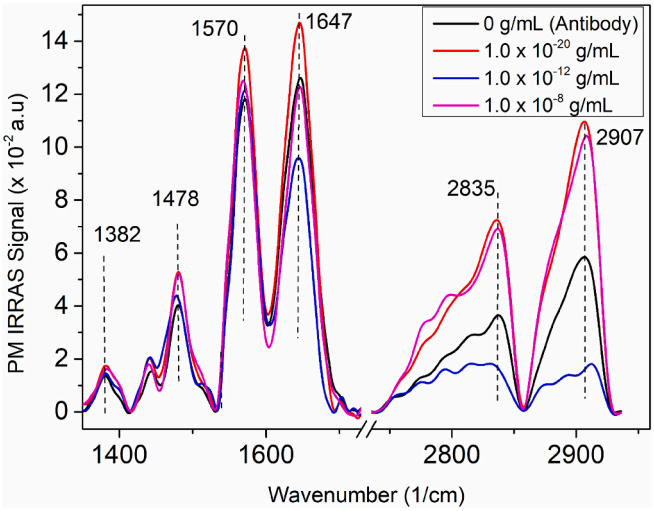

Fig. 7. Normalized PM-IRRAS spectra for the biosensors made with CMCt films for spike protein detection between 1370 and 1750 cm^{-1} and 2730-2940 cm^{-1}..

Taken together, the results reported here indicate that electrical measurements can be used with low-cost immunosensors for diagnosis of SARS-CoV-2 infection, which can be transformative in public policies for mass testing in developing countries, particularly because impedance spectroscopy measurements can be performed with portable instruments [42].

Credit statement

Juliana: Conceptualization; Data curation; Formal analysis;

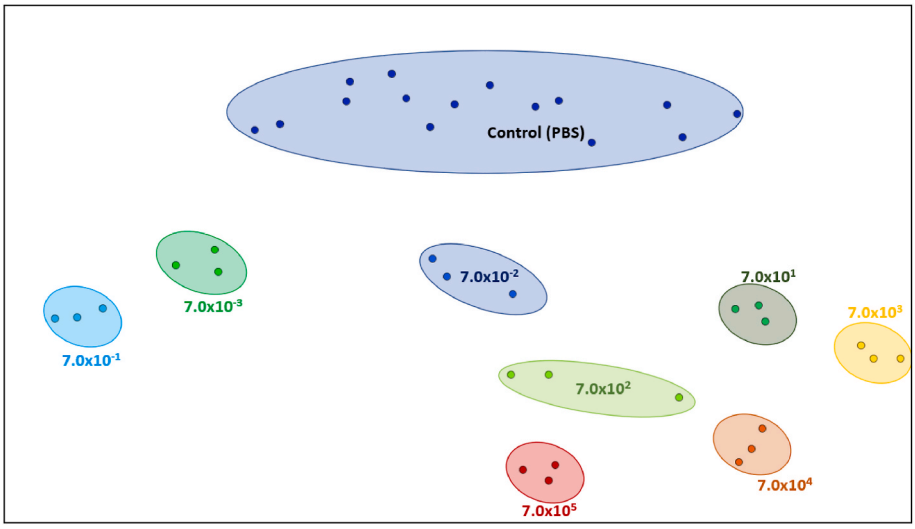

Fig. 6. IDMAP plot for the capacitance spectra obtained with the biosensor to detect inactivated SARS-CoV-2 virus at various concentrations. The cluster at the top of the map, marked with "Control", refers to a PBS solution without SARS-CoV-2. There is a trend for the data points related to the inactivated virus samples to be located to the right and to the bottom on the map with increasing concentrations.

Investigation; Methodology; Project administration; Writing – review & editing. (responsible to performed experiments, data analysis, prepared the figures and wrote the manuscript). Andrey: Conceptualization; Data curation; Formal analysis; Investigation; Methodology; Writing – review & editing. (responsible to performed experiments, data analysis, prepared the figures and wrote the manuscript). Monara: Formal analysis; Investigation; Methodology; Writing – review & editing the manuscript (performed the preparation and characterization of the SARS-CoV-2 Inactivation). José: Investigation; Methodology; Project administration; Writing – review & editing (responsible for the experiments and data analysis at State University of Campinas). Pedro: Investigation; Methodology; Project administration; Writing – review & editing (responsible for the experiments and data analysis at State University of Campinas). Luiz Henrique: Formal analysis; Investigation; Methodology; Supervision; Project administration; Writing – review & editing (responsible for the experiments and data analysis at Embrapa Instrumentation). Osvaldo: Formal analysis; Investigation; Methodology; Supervision; Funding acquisition; Project administration; Writing – review & editing (was the research coordinator and edited the manuscript). All authors proofread the manuscript.

Declaration of competing interest

The authors declare that they have no known competing financial interests or personal relationships that could have appeared to influence the work reported in this paper.

Acknowledgments

This work was supported by National Council for Scientific and Technological Development (CNPq) (Grant #103266/2020-8), São Paulo Research Foundation (FAPESP) (Grants # 2020/04579-7, 2020/08744-2, 2018/18953-8 and 2018/22214-6), SISNANO (MCTI) and Agronano Network. The authors also are grateful to CNPEM researchers Maria Helena Piazzetta and Angelo Gobbi for their assistance in electrode fabrication.

Appendix A. Supplementary data

Supplementary data to this article can be found online at https://doi.org/10.1016/j.talanta.2021.123076.

References

[1] N. Zhu, D. Zhang, W. Wang, X. Li, B. Yang, J. Song, X. Zhao, B. Huang, W. Shi, R. Lu, P. Niu, F. Zhan, X. Ma, D. Wang, W. Xu, G. Wu, G.F. Gao, W. Tan, A novel coronavirus from patients with pneumonia in China, 2019, N. Engl. J. Med. 382 (2020) 727–733, https://doi.org/10.1056/NEJMoa2001017.

[2] Y. Huang, C. Yang, X. Xu, W. Xu, S. Liu, Structural and functional properties of SARS-CoV-2 spike protein: potential antivirus drug development for COVID-19, Acta Pharmacol. Sin. 41 (2020) 1141–1149, https://doi.org/10.1038/s41401-020-0485-4.

[3] C. Wang, Z. Wang, G. Wang, J.Y.-N. Lau, K. Zhang, W. Li, COVID-19 in early 2021: current status and looking forward, Signal Transduct. Target. Ther. 6 (2021) 114, https://doi.org/10.1038/s41392-021-00527-1.

[4] I.A. Mattioli, A. Hassan, O.N. Oliveira Jr, F.N. Crespilho, On the challenges for the diagnosis of SARS-CoV-2 based on a review of current methodologies, ACS Sens. 5 (2020) 3655–3677, https://doi.org/10.1021/acssensors.0c01382.

[5] R. Lu, X. Zhao, J. Li, P. Niu, B. Yang, H. Wu, W. Wang, H. Song, B. Huang, N. Zhu, Y. Bi, X. Ma, F. Zhan, L. Wang, T. Hu, H. Zhou, Z. Hu, W. Zhou, L. Zhao, J. Chen, Y. Meng, J. Wang, Y. Lin, J. Yuan, Z. Xie, J. Ma, W.J. Liu, D. Wang, W. Xu, E. C. Holmes, G.F. Gao, G. Wu, W. Chen, W. Shi, W. Tan, Genomic characterisation and epidemiology of 2019 novel coronavirus: implications for virus origins and receptor binding, Lancet 395 (2020) 565–574, https://doi.org/10.1016/S0140-6736(20)30251-8.

[6] A. Nitsche, B. Schweiger, H. Ellerbrok, M. Niedrig, G. Pauli, SARS coronavirus detection, Emerg. Infect. Dis. 10 (2004) 1300–1303, https://doi.org/10.3201/eid1007.030678.

[7] R. Kubina, A. Dziedzic, Molecular and serological tests for COVID-19. A comparative review of SARS-CoV-2 coronavirus laboratory and point-of-care diagnostics, Diagnostics 10 (2020) 434, https://doi.org/10.3390/diagnostics10060434.

[8] L. Falzone, G. Gattuso, A. Tsatsakis, D. Spandidos, M. Libra, Current and innovative methods for the diagnosis of COVID-19 infection (Review), Int. J. Mol. Med. 47 (2021) 100, https://doi.org/10.3892/ijmm.2021.4933.

[9] J.C. Soares, A.C. Soares, V. da C. Rodrigues, P.R.A. Oiticica, P.A. Raymundo-Pereira, J.L. Bott-Neto, L.A. Buscaglia, L. Castro, L.C. Ribas, L. Scabini, L. C. Brazaca, D. Correa, L.H. Mattoso, M.C.F de Oliveira, A.C.P.L.F. de Carvalho, E. Carrilho, O.M. Bruno, M.E. Melendez, O. N Oliveira Jr, Detection of a SARS-CoV-2 sequence with genosensors using data analysis based on information visualization and machine learning techniques, Mater. Chem. Front. (2021), https://doi.org/10.1039/D1QM00665G, 10.1039.D1QM00665G.

[10] E.S. Winkler, A.L. Bailey, N.M. Kafai, S. Nair, B.T. McCune, J. Yu, J.M. Fox, R. E. Chen, J.T. Earnest, S.P. Keeler, J.H. Ritter, L.-I. Kang, S. Dort, A. Robichaud, R. Head, M.J. Holtzman, M.S. Diamond, SARS-CoV-2 infection of human ACE2-transgenic mice causes severe lung inflammation and impaired function, Nat. Immunol. 21 (2020) 1327–1335, https://doi.org/10.1038/s41590-020-0778-2.

[11] X. Xue, J. Shi, H. Xu, Y. Qin, Z. Yang, S. Feng, D. Liu, L. Jian, L. Hua, Y. Wang, Q. Zhang, X. Huang, X. Zhang, X. Li, C. Chen, J. Guo, W. Tang, J. Liu, Dynamics of binding ability prediction between spike protein and human ACE2 reveals the adaptive strategy of SARS-CoV-2 in humans, Sci. Rep. 11 (2021) 3187, https://doi.org/10.1038/s41598-021-82938-2.

[12] M. Zhang, X. Li, J. Pan, Y. Zhang, L. Zhang, C. Wang, X. Yan, X. Liu, G. Lu, Ultrasensitive detection of SARS-CoV-2 spike protein in untreated saliva using SERS-based biosensor, Biosens. Bioelectron. 190 (2021) 113421, https://doi.org/10.1016/j.bios.2021.113421.

[13] J. Zhang, X. Fang, Y. Mao, H. Qi, J. Wu, X. Liu, F. You, W. Zhao, Y. Chen, L. Zheng, Real-time, selective, and low-cost detection of trace level SARS-CoV-2 spike-protein for cold-chain food quarantine, Npj Sci. Food. 5 (2021) 12, https://doi.org/10.1038/s41538-021-00094-3.

[14] S. Mavrikou, G. Moschopoulou, V. Tsekouras, S. Kintzios, Development of a portable, ultra-rapid and ultra-sensitive cell-based biosensor for the direct detection of the SARS-CoV-2 S1 spike protein antigen, Sensors 20 (2020) 3121, https://doi.org/10.3390/s20113121.

[15] A. Ahmadivand, B. Gerislioglu, Z. Ramezani, A. Kaushik, P. Manickam, S. A. Ghoreishi, Femtomolar-level detection of SARS-CoV-2 spike proteins using toroidal plasmonic metasensors, ArXiv200608536 Phys. (2020). http://arxiv.org/abs/2006.08536. (Accessed 22 June 2021).

[16] B. Mojsoska, S. Larsen, D.A. Olsen, J.S. Madsen, I. Brandslund, F.A. Alatraktchi, Rapid SARS-CoV-2 detection using electrochemical immunosensor, Sensors 21 (2021) 390, https://doi.org/10.3390/s21020390.

[17] V.J. Vezza, A. Butterworth, P. Lasserre, E.O. Blair, A. MacDonald, S. Hannah, C. Rinaldi, P.A. Hoskisson, A.C. Ward, A. Longmuir, S. Setford, E.C.W. Farmer, M. E. Murphy, D.K. Corrigan, An electrochemical SARS-CoV-2 biosensor inspired by glucose test strip manufacturing processes, Chem. Commun. 57 (2021) 3704–3707, https://doi.org/10.1039/D1CC00936B.

[18] Z. Rahmati, M. Roushani, H. Hosseini, H. Choobin, Electrochemical immunosensor with Cu2O nanocube coating for detection of SARS-CoV-2 spike protein, Microchim. Acta 188 (2021) 105, https://doi.org/10.1007/s00604-021-04762-9.

[19] R. Minghim, F.V. Paulovich, A. de Andrade Lopes, in: R.F. Erbacher, J.C. Roberts, M.T. Gröhn, K. Börner (Eds.), Content-based Text Mapping Using Multi-Dimensional Projections for Exploration of Document Collections, 2006, p. 60600S, https://doi.org/10.1117/12.650880. San Jose, CA.

[20] E.I. Patterson, T. Prince, E.R. Anderson, A. Casas-Sanchez, S.L. Smith, C. Cansado-Utrilla, T. Solomon, M.J. Griffiths, Á. Acosta-Serrano, L. Turtle, G.L. Hughes, Methods of inactivation of SARS-CoV-2 for downstream biological assays, J. Infect. Dis. 222 (2020) 1462–1467, https://doi.org/10.1093/infdis/jiaa507.

[21] R. Zeng, W. Wang, M. Chen, Q. Wan, C. Wang, D. Knopp, D. Tang, CRISPR-Cas12a-driven MXene-PEDOT:PSS piezoresistive wireless biosensor, Nanomater. Energy 82 (2021) 105711, https://doi.org/10.1016/j.nanoen.2020.105711.

[22] J. Chen, P. Tong, L. Huang, Z. Yu, D. Tang, Ti3C2 MXene nanosheet-based capacitance immunoassay with tyramine-enzyme repeats to detect prostate-specific antigen on interdigitated micro-comb electrode, Electrochim. Acta 319 (2019) 375–381, https://doi.org/10.1016/j.electacta.2019.07.010.

[23] Z. Yu, G. Cai, X. Liu, D. Tang, Pressure-based biosensor integrated with a flexible pressure sensor and an electrochromic device for visual detection, Anal. Chem. 93 (2021) 2916–2925, https://doi.org/10.1021/acs.analchem.0c04501.

[24] J.C. Soares, F.M. Shimizu, A.C. Soares, L. Caseli, J. Ferreira, O.N. Oliveira Jr, Supramolecular control in nanostructured film architectures for detecting breast cancer, ACS Appl. Mater. Interfaces 7 (2015) 11833–11841, https://doi.org/10.1021/acsami.5b03761.

[25] R.G. Greenler, Infrared study of adsorbed molecules on metal surfaces by reflection techniques, J. Chem. Phys. 44 (1966) 310–315, https://doi.org/10.1063/1.1726462.

[26] W. Golden, A method for measuring infrared reflection?Absorption spectra of molecules adsorbed on low-area surfaces at monolayer and submonolayer concentrations, J. Catal. 71 (1981) 395–404, https://doi.org/10.1016/0021-9517(81)90243-8.

[27] A.C. Soares, J.C. Soares, V.C. Rodrigues, O.N. Oliveira Jr, L.H. Capparelli Mattoso, Controlled molecular architectures in microfluidic immunosensors for detecting Staphylococcus aureus, Analyst 145 (2020) 6014–6023, https://doi.org/10.1039/D0AN00714E.

[28] L.S.F. Leite, S. Bilatto, R.T. Paschoalin, A.C. Soares, F.K.V. Moreira, O.N. Oliveira Jr, L.H.C. Mattoso, J. Bras, Eco-friendly gelatin films with rosin-grafted cellulose nanocrystals for antimicrobial packaging, Int. J. Biol. Macromol. 165 (2020) 2974–2983, https://doi.org/10.1016/j.ijbiomac.2020.10.189.

[29] E.A. Monyoncho, V. Zamlynny, T.K. Woo, E.A. Baranova, The utility of polarization modulation infrared reflection absorption spectroscopy (PM-IRRAS) in surface and

in situ studies: new data processing and presentation approach, Analyst 143 (2018) 2563–2573, https://doi.org/10.1039/C8AN00572A.

[30] F.V. Paulovich, M.L. Moraes, R.M. Maki, M. Ferreira, O.N. Oliveira Jr, M.C.F. de Oliveira, Information visualization techniques for sensing and biosensing, Analyst 136 (2011) 1344, https://doi.org/10.1039/c0an00822b.

[31] E. Barsoukov, J.R. Macdonald, Impedance Spectroscopy Theory, Experiment, and Applications, Wiley-Interscience, Hoboken, N.J., 2005. http://site.ebrary.com/id/10114201. (Accessed 22 June 2021).

[32] V.F. Lvovich, Impedance Spectroscopy: Applications to Electrochemical and Dielectric Phenomena, Wiley, Hoboken, N.J, 2012.

[33] D.M. Taylor, A.G. Macdonald, AC admittance of the metal/insulator/electrolyte interface, J. Phys. Appl. Phys. 20 (1987) 1277–1283, https://doi.org/10.1088/0022-3727/20/10/010.

[34] A. Inselberg, B. Dimsdale, Parallel coordinates: a tool for visualizing multi-dimensional geometry, in: Proc. First IEEE Conf. Vis. Vis. 90, IEEE Comput. Soc. Press, San Francisco, CA, USA, 1990, pp. 361–378, https://doi.org/10.1109/VISUAL.1990.146402.

[35] A.C. Soares, J.C. Soares, F.M. Shimizu, M.E. Melendez, A.L. Carvalho, O.N. Oliveira Jr, Controlled film architectures to detect a biomarker for pancreatic cancer using impedance spectroscopy, ACS Appl. Mater. Interfaces 7 (2015) 25930–25937, https://doi.org/10.1021/acsami.5b08666.

[36] A. Barth, The infrared absorption of amino acid side chains, Prog. Biophys. Mol. Biol. 74 (2000) 141–173, https://doi.org/10.1016/S0079-6107(00)00021-3.

[37] N.B. Colthup, L.H. Daly, S.E. Wiberley, Introduction to Infrared and Raman Spectroscopy, third ed., Academic Press, Boston, 1990.

[38] A. Wieckowski, C. Korzeniewski, B. Braunschweig, Vibrational Spectroscopy at Electrified Interfaces, 2013. https://nbn-resolving.org/urn:nbn:de:101:1-201502084436. (Accessed 22 June 2021).

[39] L. Zhang, M. Xiao, Y. Wang, S. Peng, Y. Chen, D. Zhang, D. Zhang, Y. Guo, X. Wang, H. Luo, Q. Zhou, Y. Xu, Fast screening and primary diagnosis of COVID-19 by ATR–FT-IR, Anal. Chem. 93 (2021) 2191–2199, https://doi.org/10.1021/acs.analchem.0c04049.

[40] A. Barth, Infrared spectroscopy of proteins, Biochim. Biophys. Acta BBA - Bioenerg. 1767 (2007) 1073–1101, https://doi.org/10.1016/j.bbabio.2007.06.004.

[41] L. Vieira, R. Schennach, B. Gollas, In situ PM-IRRAS of a glassy carbon electrode/deep eutectic solvent interface, Phys. Chem. Chem. Phys. 17 (2015) 12870–12880, https://doi.org/10.1039/C5CP00070J.

[42] L.A. Buscaglia, O.N. Oliveira Jr, J.P. Carmo, Roadmap for electrical impedance spectroscopy for sensing: a tutorial, IEEE Sensor. J. (2021), https://doi.org/10.1109/JSEN.2021.3085237, 1–1.